PHYSICAL REVIEW B **108**, 045411 (2023)

Strain-dependent electronic and mechanical properties in one-dimensional topological insulator Nb_4SiTe_4

Siyuan Liu,[1] Huabing Yin,[1,*] and Peng-Fei Liu[2,3,†]

[1] *Joint Center for Theoretical Physics, Institute for Computational Materials Science, and International Joint Research Laboratory of New Energy Materials and Devices of Henan Province, School of Physics and Electronics, Henan University, Kaifeng 475004, China*
[2] *Institute of High Energy Physics, Chinese Academy of Sciences, Beijing 100049, China*
[3] *Spallation Neutron Source Science Center, Dongguan 523803, China*

(Received 19 July 2022; revised 12 March 2023; accepted 10 July 2023; published 18 July 2023)

Topological insulators hold great promise for dissipationless transport devices due to the robust gapless states inside the insulating bulk gap. So far, several generations of topological insulators have been theoretically predicted and experimentally confirmed, most of them based on three- or two-dimensional materials. Here, on the basis of the first-principles calculations, we predict a quasi-one-dimensional (quasi-1D) topological insulator Nb_4SiTe_4 that can be prepared by exfoliation from its three-dimensional bulk phase. This material, characterized by topological $\mathbb{Z}_2$ invariants and robust zero-energy edge states, has a large nontrivial gap of ~93.6 meV, large enough for inhibiting the possibility of the thermal disturbance. Additionally, when applying pressure, we find there is an abnormal force releasing stage originating from the shrinking of the inner Nb atomic rings. In addition, we find that substrate, stacking, defect, and structure deformation have specific effects on electronic properties. Our results reveal a promising quasi-1D topological insulator Nb_4SiTe_4 and uncover its unique strain-dependent electronic and mechanical properties.

DOI: 10.1103/PhysRevB.108.045411

I. INTRODUCTION

Since the discovery of the quantum spin Hall effect [1], topological insulators (TIs), holding nontrivial edge states protected from backscattering, are revolutionizing condensed matter physics and materials science due to their topological bands and potential applications in dissipationless devices [2–7]. In the following experiment, alloying $Bi_{1-x}Sb_x$ has been verified as the first three-dimensional (3D) TI possessing metallic Dirac states on the surface of an insulating bulk [8], which is first proposed in theory [9]. Subsequently, plenty of TI candidates are discovered, such as the Bi_2Se_3 series [10–12], Li_2AsSb series [13], (Pb,Sn)Te series [14], HgTe/CdTe quantum well [15], and modified graphene [16–18]. These disruptive discoveries of record TI materials greatly promote the development of topological-insulator based electronics.

As we know, with the dimension reducing, plenty of novel mechanical properties emerge in materials, such as high elastic criterion, great anelasticity, and significant superplasticity [19]. So far, many TI candidates have been predicted theoretically and confirmed experimentally based on 2D or 3D materials. The research of 1D TIs mostly focus on the model in theory [20,21], while theoretical predictions and experimental demonstrations of real 1D TI materials are still inadequate. To date, the proposed 1D TI candidates possess various flaws, such as the extrinsic TI phase [22], small bulk band gap [23], and structural instability [24,25], which profoundly limits future applications. Thus, it is very important to explore new 1D TI materials in experiment and theory.

Recently, it is demonstrated that ternary van der Waals (vdW) materials $Nb_xSi_yTe_z$ with different stoichiometric ratio possess multifunctional promises for quantum computation [26,27], infrared detector [28], field effect transistors [29], and thermoelectricity [30]. For instance, 2D Nb_3SiTe_6 is predicted to be a nodal-line semimetal and exhibits a strongly suppressed electron-phonon interaction [27]. Nb_2SiTe_4 has a stable narrow gap and is promising for midinfrared detection [28]. In the case of $NbSi_{0.45}Te_2$, angle-resolved photoemission spectroscopy demonstrates the existence of nonsymmorphic protected 1D directional massless Dirac fermions, which stems from a striplike structural modulation [26]. When the stoichiometric ratio is confined in the form of $Nb_2Si_{x-1}Te_4$ ($5/3 < x < 2$), it is metallic along the chain direction and exhibits a semiconducting feature perpendicular to the chain direction [29]. As a member of this series, the synthesized Nb_4SiTe_4 shares the same atomic geometry as Ta_4SiTe_4 [31], whose 1D geometry is verified to be a TI in our previous work [32]. In this work, we theoretically investigate the electronic, mechanical, and electromechanical properties of quasi-one-dimensional (quasi-1D) Nb_4SiTe_4, which could be exfoliated from its bulk counterparts. We verify that quasi-1D Nb_4SiTe_4 is an intrinsic $\mathbb{Z}_2$ TI with a large bulk band gap of ~93.6 meV. The degenerated edge states are robust against the H decorations but limited by the length of nanowire. By applying external strain, an unexpected force releasing stage appears with the Dirac band gap opening again, which could

---

[*] yhb@henu.edu.cn
[†] pfliu@ihep.ac.cn

be ascribed to the different shrinking ratio of the inner Nb and outer Te atom tubes. Meanwhile, it shows robust TI characteristics against external strain less than 7%. In addition, we find that defect, stacking, and structure deformation are extremely vital for electronic properties. Our work will therefore be of considerable interest to stimulate experimental studies on the quantum spin Hall effect in quasi-1D TI Nb_4SiTe_4.

II. COMPUTATIONAL METHODS

The first-principles calculations were implemented in the Vienna *ab initio* simulation package (VASP) based on density functional theory (DFT) [33,34]. The generalized gradient approximation of Perdew-Burke-Ernzerhof was employed to treat the exchange-correlation potentials [35], while the projector augmented-wave method was used to treat the ionic potentials [36]. To describe the vdW interactions precisely, the DFT-D3 method [37] was employed throughout the first-principles calculations. For quasi-1D Nb_4SiTe_4, the vacuum buffer space was set to be more than 20 Å to prevent the interaction between the adjacent nanowires. Additionally, the first Brillouin zone was sampled by the 1 × 1 × 10 Γ-centered Monkhorst-Pack *k*-point grid. A kinetic-energy cutoff of 500 eV was employed to expand the plane-wave basis set. The energy convergence criterion was chosen as 10^{-6} eV between two ionic steps, and the force convergence criterion allowed on each atom was chosen as 0.01 eV/Å. The phonon spectrum was calculated within the finite-displacement method on a 1 × 1 × 5 supercell as implemented in the PHONOPY package [38]. The *ab initio* molecular dynamics (AIMD) simulations were implemented on a 1 × 1 × 5 supercell within the canonical ensemble using the Nosé-Hoover thermostat in constant volume and temperature [39,40]. The VASP2WANNIER90 interface [41] and the WANNIER90 package [42] were employed to obtain the maximally localized Wannier functions (MLWFs) and parametrize the tight-binding (TB) Hamiltonian matrix elements. The WANNIERTOOLS package [43] was used to obtain the surface band structures and the Zak phase based on the TB Hamiltonian. The band unfolding is obtained via the VASPKIT package [44].

III. RESULTS AND DISCUSSION

A. Crystal structure and stability

The bulk metal telluride compound Nb_4SiTe_4 has been experimentally synthesized [31,45] as a naturally quasi-1D vdW material in Fig. 1(a). It forms in the orthorhombic space group *Pbma* (No. 55). Each unit cell is composed of two quasi-1D Nb_4SiTe_4 nanowires parallely arranged along the *z* axis by the vdW interactions. The optimized lattice constants are $a = 18.0$ Å, $b = 10.5$ Å, and $c = 4.8$ Å, which agree well with the previous experimental results of $a = 18.2$ Å, $b = 10.5$ Å, and $c = 4.8$ Å [45]. Nb_4SiTe_4 is constructed by the antiprismatically stacked Nb_4Te_4 monomers with Si atoms occupying the interspaces in Fig. 1(b) [31,46,47]. As shown in the left panel of Fig. 1(c), the Nb_4Te_4 monomer is formed by the Te corner-sharing square monomer with Nb atoms as bridges into networks. In order to quantify the feasibility of exfoliating quasi-1D Nb_4SiTe_4 from its bulk phase, we calculate the exfoliation energy [48] by

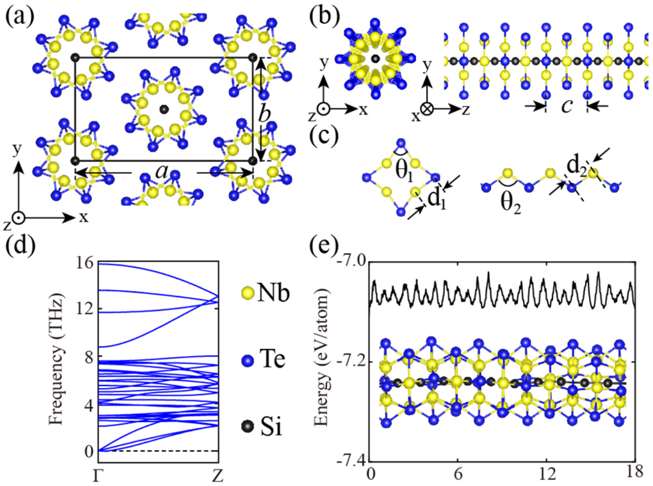

FIG. 1. (a) Top view of 3D Nb_4SiTe_4 bulk and (b) side view of quasi-1D Nb_4SiTe_4. The yellow, blue, and black balls represent Nb, Te, and Si atoms, respectively. The *a*, *b*, and *c* are corresponding lattice constants. (c) The schematic of bonding between the Nb and Te atoms perpendicular to (left) and along the extended direction, where *d* and *θ* represent the nearest distance between them and the angle of Te-Nb-Te respectively. (d) Phonon spectrum and (e) the energy evolutions from AIMD simulations of quasi-1D Nb_4SiTe_4. Inset in Fig. 1(e): The side view of quasi-1D Nb_4SiTe_4 nanowire after 18 ps AIMD simulations.

$$E_{\text{exf}} = \frac{E_{\text{bulk}}}{N_{\text{bulk}}} - \frac{E_{ID}}{N_{ID}}, \tag{1}$$

where the *E* and *N* represent the total energy and number of atoms, respectively. E_{exf} is calculated to be 116.9 meV/atom, which is much smaller than the exfoliation energy of the synthesized 1D Te atomic chain (273.0 meV/atom) [49]. This implies that it is reasonable to obtain the Nb_4SiTe_4 nanowire from its bulk counterpart. In Fig. 1(b), the optimized lattice constant is 4.83 Å for quasi-1D Nb_4SiTe_4. It crystallizes in the space group of *P*4/*mmm* (No. 123) with all atoms being at the Wyckoff position 16*g* site. The Nb-Te bond lengths are $d_1 = 2.92$ Å in the plane and $d_2 = 2.84$ Å along the *z* axis. The Te-Nb-Te angle is 111.5° in the plane and 160.3° along the *z* axis. These values are approximate to those of bulk Nb_4SiTe_4 in Table I. To confirm the stability of quasi-1D Nb_4SiTe_4, we compute its phonon spectrum in Fig. 1(d). The absence of imaginary phonon mode over the first Brillouin zone guarantees the optimized structure located at the minimum on the potential-energy surface. The maximum frequency reaches up to 15.6 THz (520.4 cm^{-1}), implying a

TABLE I. The lattice constants (*a*, *b*, and *c* in Å), Nb-Te distances (d_1 and d_2 in Å), and Te-Nb-Te angle (θ_1 and θ_2) for the bulk and quasi-1D Nb_4SiTe_4.

	a	b	c	d_1	d_2	θ_1	θ_2
Bulk	18.0	10.5	4.80	2.92	2.85	110.7	159.0
1D			4.83	2.92	2.84	111.5	160.3

TABLE II. The charge transfers (CTs) (in e) between atoms in the quasi-1D Nb_4SiTe_4 nanowire.

Atom	CTs	Atom	CTs	Atom	CTs
Nb1	−0.89	Nb7	−0.90	Te3	+0.63
Nb2	−0.89	Nb8	−0.90	Te4	+0.63
Nb3	−0.89	Si1	+1.05	Te5	+0.63
Nb4	−0.89	Si2	+1.05	Te6	+0.63
Nb5	−0.90	Te1	+0.64	Te7	+0.63
Nb6	−0.90	Te2	+0.64	Te8	+0.63

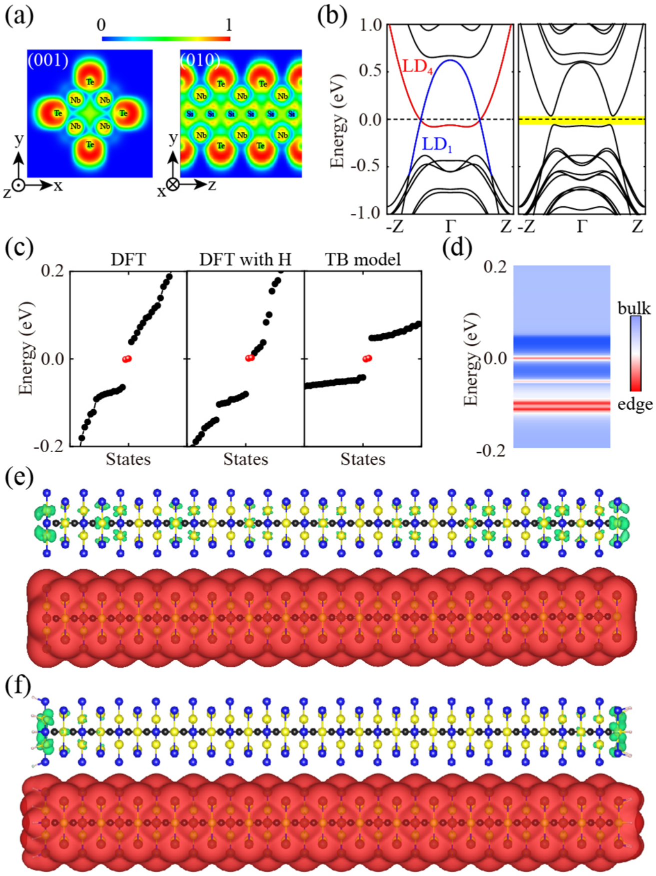

FIG. 2. (a) The electron localization function and (b) calculated band structures without (left panel) and with (right panel) spin-orbit coupling for quasi-1D Nb_4SiTe_4. The red LD_4 and blue LD_1 represent the irreps of the corresponding bands. (c) The discrete energy levels of finite-size Nb_4SiTe_4 nanowire. (d) The calculated energy spectrum of the semi-infinite Nb_4SiTe_4 nanowire based on the iterative Green's functions. The distributions of the zero-energy (upper panel) and bulk (lower panel) states of the finite-size Nb_4SiTe_4 nanowire without (e) and with (f) H decorations based on the DFT calculations.

strong atomic interaction in quasi-1D Nb_4SiTe_4 [50–54]. The kinetic stability is also confirmed by AIMD simulations at 300 K for 18 ps. The energy oscillates in a tiny interval and the structure is well retained without obvious structure distortion during the simulation in Fig. 1(e). Based on the above results, we conclude that quasi-1D Nb_4SiTe_4 is reasonable to exist stably.

B. Electronic and topological properties

Based on Bader charge [55] analysis, each Nb atom loses 0.9 electrons, one Si atom obtains 1.05 electrons, and one Te atom obtains 0.6 electrons in Table II. Although the electronegativity of Si (37.3 ± 7) is close to Te (38 ± 4) [56], their charge transfers are different due to the atomic arrangement. In one primitive cell, each Si atom is surrounded by eight Nb atoms, whereas each Te atom is fourfold coordinated to Nb atoms. This gives rise to the fact that the charge transfer of Si atoms is twice as much as that of Te atoms. To explore the nature of chemical bonding, the electron localization functions (ELFs) [57] are calculated in Fig. 2(a). In the (001) plane, the interactions between Nb and Te atoms are ionic, which is verified by the virtually spherical structure of ELF around each atom and the low ELF intervening regions. The interactions between Si atoms are covalent due to the appearance of high ELF values in intervening regions. In addition, three-center bonding appears between Nb and Si atoms [58].

We now turn to the discussion of the electronic structures of quasi-1D Nb_4SiTe_4. In Fig. 2(b), the conduction and valance bands overlap around the Fermi level, forming the inversion band structures. To understand the mechanism of band inversion, we calculate the irreducible representations (irreps) of the two bands. As shown in the left panel of Fig. 2(b), the red band carries the LD_4 irrep while the blue one has the LD_1 irrep, which results in the band inversion protected by the $\{m_{100}|0\}$, $\{m_{010}|0\}$, $\{m_{110}|0\}$, and $\{m_{1-10}|0\}$ mirror symmetry operations. In the vicinity of the Fermi level, the two linear dispersed bands produce intrinsic Dirac cones [59]. As shown in Fig. 3, the Fermi level is derived from hybridized states of the Nb $d_{z^2,xz,yz}$ orbitals and the Te $p_{x,y}$ orbitals. When spin-orbit coupling (SOC) is taken into consideration, the degenerate Dirac states are damaged with an enlarged global band gap E_g of ∼93.6 meV in the right panel of Fig. 2(b). This value is larger than the experimentally verified 2D TIs $1T'-MX_2$ ($M =$ W, Mo and $X =$ Te, Se, S) [60,61] and quasi-1D TIs $\beta-Bi_4I_4$ [23]. When considering the SOC effect stemming from a single element, the opened E_g are weakened to 79.1, 31.1, and 11.3 eV for Te, Nb, and Si element, respectively, in Fig. 4. It indicates Te and Nb atoms dominate the SOC in opening E_g.

As proposed in previous theoretical work [4,5,62–64], the relativistic SOC effect can forge the nontrivial topological order of bands via opening E_g between inversed bands, which

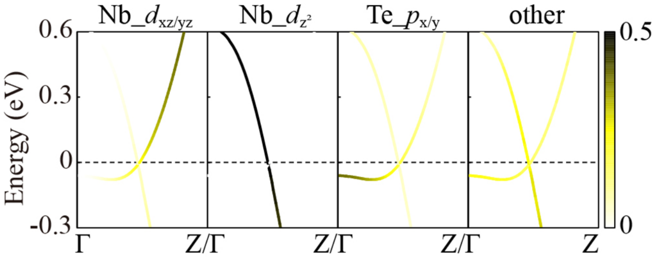

FIG. 3. The orbital angular momentum projected band structures of quasi-1D Nb_4SiTe_4.

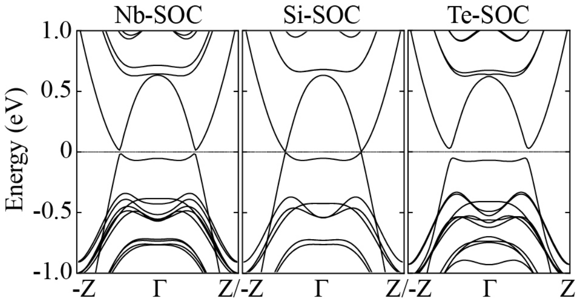

FIG. 4. The band structures of quasi-1D Nb_4SiTe_4 with SOC from individual element.

is essential for TIs. As a global feature of TIs, it can be directly classified by the $\mathbb{Z}_2$ topological invariant ν for the inversion system by

$$(-1)^{\nu} = \prod_{i=1}^{n} \delta(k_i), \tag{2}$$

where $\delta(k_i)$ is the product of the parity eigenvalues $\xi(i)$ for the occupied bands (N) at these time-reversal-invariant momenta (TRIM). The detailed parities of occupied bands for quasi-1D Nb_4SiTe_4 are listed in Table III. It yields $\nu = 1$, indicating the nontrivial band topology in quasi-1D Nb_4SiTe_4. In order to verify our results, we perform topological calculations using the tight-binding Wannier orbital based Hamiltonian [65] for quasi-1D Nb_4SiTe_4. Figure 5 displays the Wannier interpolated and DFT bands. The Zak phase [66] is calculated via integrating the Berry connection across the 1D Brillouin zone by $\gamma_n = i\int_{-\pi/c}^{\pi/c} dk \langle u_{nk}|\partial_k|u_{nk}\rangle$, where the $|u_{nk}\rangle$ comes from the MLWFs. The ν is computed, by $(-1)^{\nu} = e^{i\sum_{i=1}^{n}\gamma_n}$, to be 1, which agrees with the above value calculated from DFT data. To deeply understand the SOC induced nontrivial topological phase, we also construct an effective TB model based on atomic orbitals

$$H_{TB} = \sum_{i,\alpha} \varepsilon_i^{\alpha} c_i^{\alpha+} c_i^{\alpha} + \sum_{\langle i,j\rangle,\alpha,\beta} t_{ij}^{\alpha\beta}\left(c_i^{\alpha+} c_j^{\beta} + \text{H.c.}\right) + \lambda \boldsymbol{S} \cdot \boldsymbol{L}, \tag{3}$$

where ε_i^{α}, $c_i^{\alpha+}$, and c_i^{α} represent the on-site energy, creation, and annihilation operators of electrons at the α orbital of the ith atom, respectively. $t_{ij}^{\alpha\beta}$ and λ represent the hopping strength between them and the strength of SOC effect. The adopted parameters are $\varepsilon_1 = 0.3$, $\varepsilon_2 = 0.5$, $\varepsilon_3 = \varepsilon_4 = 1.1$, $\varepsilon_5 = \varepsilon_6 = -2.4, t_1 = t_3 = -t_2 = -t_4 = 0.3, t_5 = 2.2, t_6 = 1$, and $\lambda = 0.2$. The fitted band structures are shown in Fig. 6(b). It is clear that this model can capture the characteristic of band inversion and degenerate Dirac-like states. When including the SOC effect, the degenerate states are broken to create a band gap. Using this model, we evaluate the $\mathbb{Z}_2$ topological invariant via Zak phase. The result is $\nu = 1$, indicating nontrivial topological phase induced by the SOC effect.

TABLE III. The calculated parity eigenvalues of the occupied spin-degenerate bands vicinity at the TRIM points for quasi-1D Nb_4SiTe_4. The odd and even parities are labeled with − and +, respectively.

TRIM	Parities	Product
Γ	− + − − + − − + + + + + −	−
	+ − − − − − + − + + + + +	
	− − + − − + + − − + − − +	
Z	+ − + − + + − − + + − − +	+
	− + − + − + − + − + − + −	
	+ − + − + − + − + − + + −	

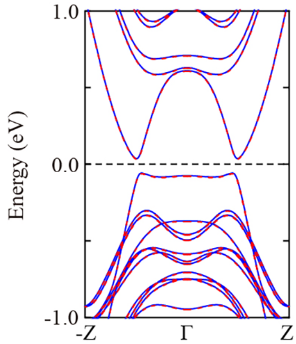

FIG. 5. The band structures of quasi-1D Nb_4SiTe_4 based on the MLWFs (blue) and DFT calculations (red).

For TIs, another notable feature is the bulk-edge correspondence [2,4,67–69], which guarantees the zero-energy states in the bulk gap. To illustrate this character, we construct a finite nanowire of 16 times primitive cell with 10 Å vacuum on both sides and calculate the corresponding discrete energy levels. In Fig. 2(c), the DFT and TB calculations give similar results, in which discrete zero-energy states marked as red dots deviate from the sequential bulk states and reside in the gap. It is also confirmed by the energy spectrum of the semi-infinite nanowire calculated using the iterative Green's functions [43] in Fig. 2(d). The charge distributions of the zero-energy and bulk states in real space are shown in Fig. 2(d), which give the character of a 1D TI satisfactorily.

In order to verify the robustness of results, the edge states of 1D finite-size nanowire are explored under different decorations and lengths. As shown in Fig. 2(c), H atoms decorated at two edges cannot eliminate the degenerated edge states that still reside in the bulk gap. In Fig. 2(f), the charge distributions of states in real space indicate that the zero-energy states are limited to edges, similar to the case without decorations.

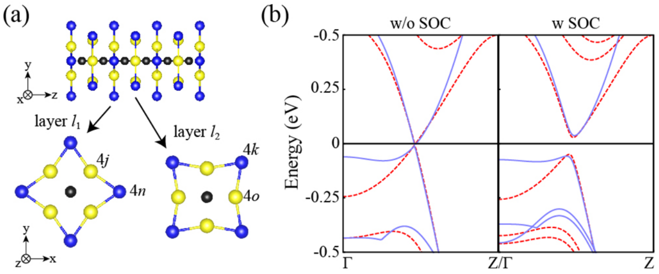

FIG. 6. (a) The Wyckoff positions of Nb (yellow balls) and Te atoms (blue balls) in quasi-1D Nb_4SiTe_4. (b) The fitted (red dashed line) and DFT (blue solid line) band structures. The black line is the Fermi level at 0 eV.

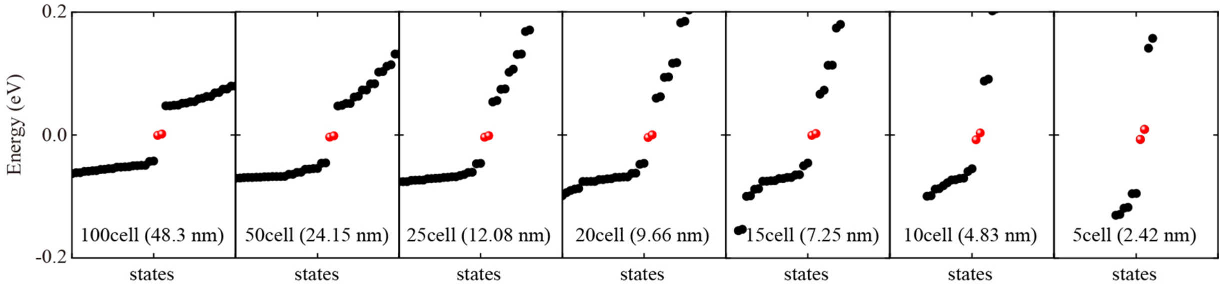

FIG. 7. The evolution of discrete energy levels for finite-size Nb_4SiTe_4 nanowire. The bulk and edge states are labeled as black and red balls, respectively.

Nevertheless, the H decorations can change significantly the position of edge states close to the conduction states. In addition, the effects of length on edge states are also explored. As shown in Fig. 7, all of the edge states reside in the bulk gap. However, as the length decreases, the degenerated edge states are opened gradually, showing the importance of length for edge states. Similar results are also observed in the 3D superconductor $\beta-Bi_2Pd$ [70].

C. Electronic and mechanical properties under strain effect

In previous work [64,71–75], the electronic states of low-dimensional materials are highly sensitive to the applied strain. Hence, it is highly considerable to explore the electronic states under strains. As shown in Fig. 8(a), E_g evenly decreases from 3.9 to 0 meV with the strain being from -3% to 7%. The corresponding band structures are calculated with and without the SOC in Fig. 8(c). The Dirac cones are well retained in the absence of SOC. As the strain increases, the Dirac points deviate from the Fermi level slightly. When SOC is included, the degenerate Dirac points separate with emerging E_g and in the range from 0% to 7%. As the strain exceeds 7%, however, the gap tends to be closed and the 1D system transforms from the nontrivial topological insulator to metal. Figure 8(b) shows band gap with variable SOC strength χ under the 0% and 7% strains. It is obvious that the E_g is positively correlated with χ, indicating the pivotal role of SOC in opening the band gap. When the strain exceeds 7%, nevertheless, the SOC cannot separate the valance and conduction bands anymore because an extra valance band is lifted to cross the Fermi level and connect the valance and conduction bands.

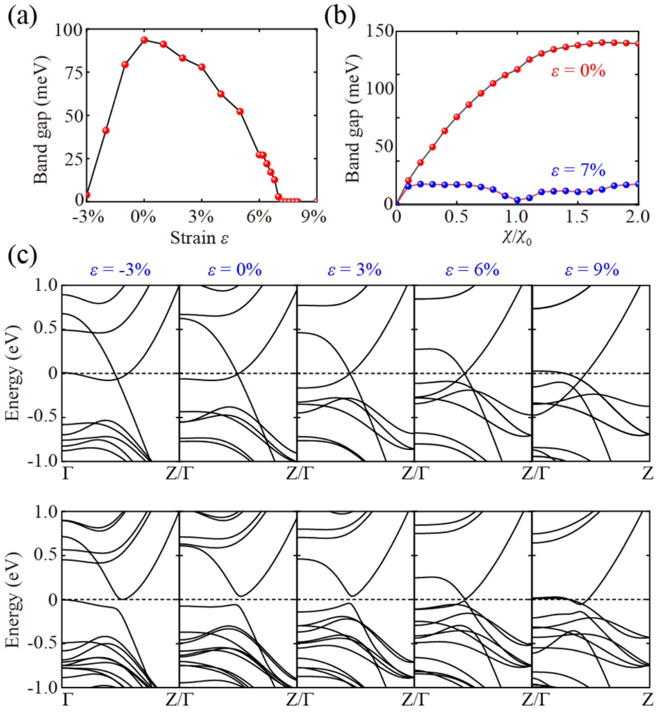

FIG. 8. (a) The global band gap E_g dependence on the strain ε for quasi-1D Nb_4SiTe_4. (b) E_g with various relative SOC strengths χ under selected strains ε. The χ_0 stands for the normal (physical) SOC strength. (c) The band structures without (upper panel) and with (lower panel) the SOC effect under selected ε. The black dashed line is the Fermi level at 0 eV.

To gain an insight into the above phenomenon, we meticulously evaluate its mechanical properties of the stretching effect along the z axis. We calculate the strain energy by $E_S = E_T(\varepsilon) - E_T(\varepsilon = 0)$, where $E_T(\varepsilon)$ represents the total energy under a given axial strain ε and $E_T(\varepsilon = 0)$ represents the total energy at equilibrium state. To balance the efficiency and accuracy, we use the $1 \times 1 \times 5$ supercell with periodic boundary conditions. The stretching strain is defined as $\varepsilon = (c - c_0)/c_0$, where c_0 and c are the equilibrium and stretched lattice constants, respectively. For each stretching strain, we fully relax the supercells and repeat calculations of the stretching energy. After that, we can obtain the tension force $F_T = -\partial E_S(\varepsilon)/\partial c$ and force constant $\kappa = \partial^2 E_S/\partial^2 c$ from the energy-strain relationships. The elastic features are characterized by the Young's modulus $Y_S = (1/c_0)(\frac{\partial^2 E_S}{\partial^2 \varepsilon})$ [76,77]. In Fig. 9(a), under strains, quasi-1D Nb_4SiTe_4 experiences three stages. I: The elastic deformation stage ($\varepsilon = -3\%$–17%); II: The plastic deformation stage ($\varepsilon = 18\%$–42%); and III: The breaking stage ($\varepsilon = 43\%$–∞).

During stage I, the E_S increases with the strain effect enhancing, while the F_T is linear with ε. This corresponds to the harmonic regime, in which the elastic deformation is invertible and the deformed nanowire can be optimized back to its initial structure via simple relaxation calculation. The Y_S is estimated to be 417.2 GPa (2.06×10^{-7} N), which is much larger than those of the flexible 1D semiconductor SnIP (190 GPa) [78], WS_2 nanotube (152 ± 68 GPa), and MoS_2 nanotube (230 GPa) [79], but smaller than that of carbon nanotubes [80] (416–1160 GPa in theory [81–83] and

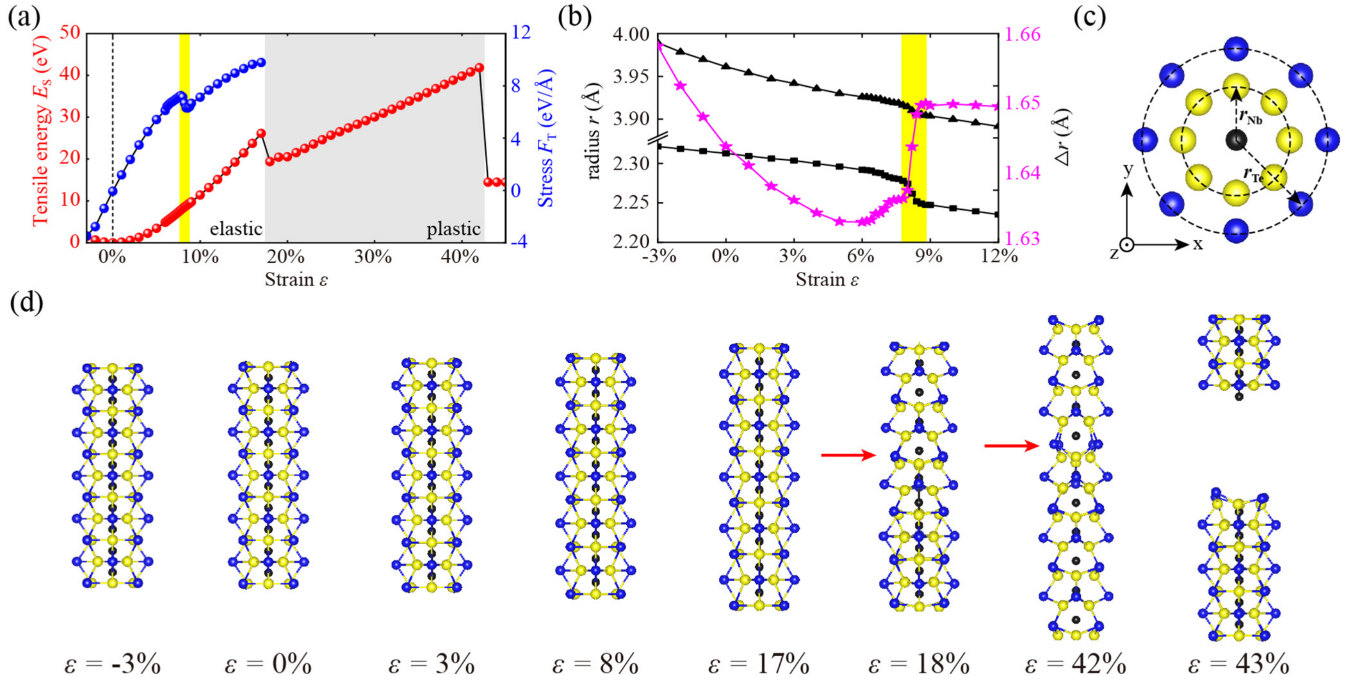

FIG. 9. (a) The strain energy E_S (red) and tension force F_T (blue) dependencies under strain ε for the quasi-1D Nb_4SiTe_4 supercell. (b) The radius of the inner Nb atoms tube (black triangles) and the outer Te atoms tube (black squares), and the difference between them (magenta stars) $\Delta r = r_{Te} - r_{Nb}$. The white, shaded, and yellow regions indicate the elastic, plastic, and force releasing stage, respectively. (c) The schematic of the inner Nb atoms and the outer Te atoms tubes. (d) The atomic geometry under selected ε. The red arrows indicate the most intense position of the quasi-1D Nb_4SiTe_4 supercell under $\varepsilon = 18\%$ and $\varepsilon = 42\%$. The yellow, black, and blue balls correspond to Nb, Si, and Te atoms, respectively.

1200 GPa in experiment [84]), implying its excellent tensile strength. The κ is 85.2 N/m, which is larger than that of silicene (30 N/m) nanoribbon [77] but much smaller than graphene (176 N/m) and BN (144 N/m) nanoribbons. The elastic stretching threshold is up to $\varepsilon = 17\%$, which is larger than that of Cu (8% [85] or 5% [86]), ZnO (6.5% [87]), and Ag nanowire (10% [88]). This value is also comparable to some well-known 1D nanotube materials, such as WS_2 nanotube (14%) and MoS_2 nanotube (17%–19%) [79]. These make it a promising 1D system with excellent mechanical properties. During this stage, although the structure undergoes no deformation, we observe an abnormal force releasing stage occurs in the range of 7.8%–8.8% in Figs. 9(a) and 10(a), which dramatically changes the relationship between F_T and ε. The energy drops at $\varepsilon = 18\%$ with the emergence of the yielding point. In stage II, the stretching strain gives rise to severe structural deformations. The Si chain is distributed nonuniformly and the Nb_4Te_4 monomers are bent in Fig. 9(d). Such deformation hinders the nanowire from returning to the equilibrium state after releasing the stretching strain. It indicates that the deformation during this stage is plastic. Stage II ends at the breaking point of $\varepsilon = 43\%$ where the E_S drops sharply and the nanowire turns into two pieces. For the generality, we also investigate the mechanical properties of its sister compound quasi-1D Ta_4SiTe_4. As shown in Fig. 11(a),

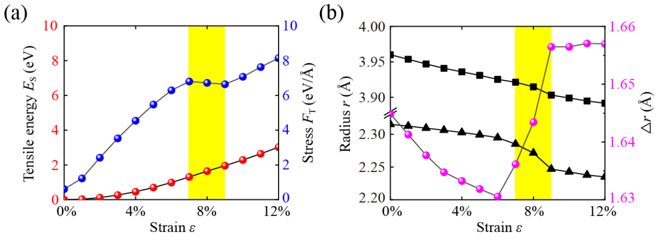

FIG. 10. (a) The strain energy E_S (red) and tension force F_T (blue) under strains for quasi-1D Nb_4SiTe_4 with primitive cell. (b) The radius of the inner Nb atoms tube (black triangles) and the outer Te atoms tube (black squares), and the difference between them (magenta balls) $\Delta r = r_{Te} - r_{Nb}$. The yellow region indicates the force releasing stage.

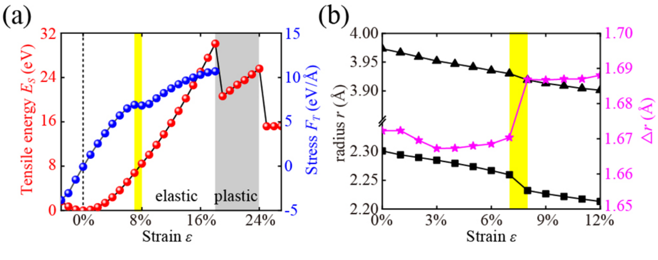

FIG. 11. (a) The strain energy E_S (red) and tension force F_T (blue) dependencies under strain ε for the quasi-1D Ta_4SiTe_4 supercell. (b) The radius of the inner Nb atoms tube (black triangles) and the outer Te atoms tube (black squares), and the difference between them (magenta stars) $\Delta r = r_{Te} - r_{Ta}$. The white, shaded, and yellow regions indicate the elastic, plastic, and force releasing stage, respectively.

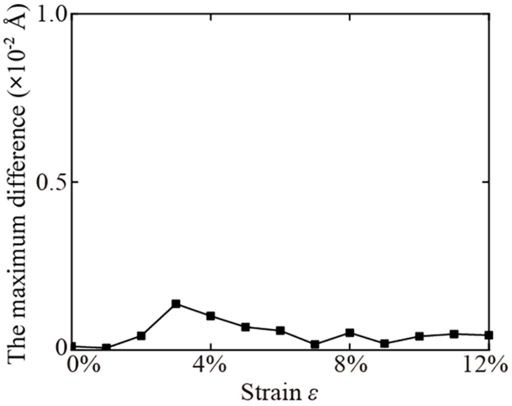

FIG. 12. The maximum differences of the distance between the nearest Nb_4Te_4 monomers for the Nb_4SiTe_4 supercell.

quasi-1D Ta_4SiTe_4 also experiences three stages: The elastic deformation stage ($\varepsilon = -3\%$–18%), the plastic deformation stage ($\varepsilon = 19\%$–24%), and the breaking stage ($\varepsilon = 25\%$–∞). During the elastic stage, the anomalous force releasing stage also occurs approximately in the range of 7%–8%. Moreover, the Y_S is estimated to be 405.2 GPa (2.01×10^{-7} N), much closer to the value of quasi-1D Nb_4SiTe_4. However, quasi-1D Ta_4SiTe_4 has a very short plastic stage, and the breaking stage occurs much in advance, implying the difference between these quasi-1D systems in large-strain deformation.

Based on the above, we know the force releasing approximately occurs after $\varepsilon = 7\%$. To uncover the origin of this abnormal force releasing stage in stage I, we carefully study the evolution of atomic geometry ranging from -3% to 12%. The minimum distance between Nb_4Te_4 monomers undulates within less than 1.5×10^{-3} Å in Fig. 12, manifesting that the nanowire is monotonously stretched along the extended direction. This does not dominate the unexpected force releasing stage. As shown in Fig. 9(c), quasi-1D Nb_4SiTe_4 can be viewed as a multiwalled nanotube of Nb and Te atoms with a monatomic Si chain being in nanotubes. Under the stretching strain, the Nb and Te nanotube radius shrinks with different rates in Figs. 9(b) and 10(b). Specifically, in the range of 0%–6%, the shrinking ratio of the outer Te nanotube is more intense than that of the inner Nb nanotube, decreasing the distance between the Nb and Te atoms. This process increases repulsion between them, making the interaction deviate from the equilibrium position. When the strain reaches 6%, the repulsion is at its maximum and begins to drive the Nb nanotube to shrink faster to remit the extra repulsion. Thus, it goes in reverse from 6% to 9%. This can be clearly shown by the radial difference $\Delta r = r_{\mathrm{Te}} - r_{\mathrm{Nb}}$. During the unexpected force releasing stage (in the range of 7.8%–8.8%), the Δr sharply increases. With the strain exceeding 8.8%, the Δr tends to a constant. For quasi-1D Ta_4SiTe_4, the similar movement of atoms also occurs in the range of $\varepsilon = 7\%$–8%, as shown in Fig. 11(b), although they own different atomic numbers. Thus, we consider the shrinking ratio of outer and inner nanotubes accounts for the origin of the abnormal force releasing stage. This phenomenon is only related to the atomic structures, independent of the atomic numbers.

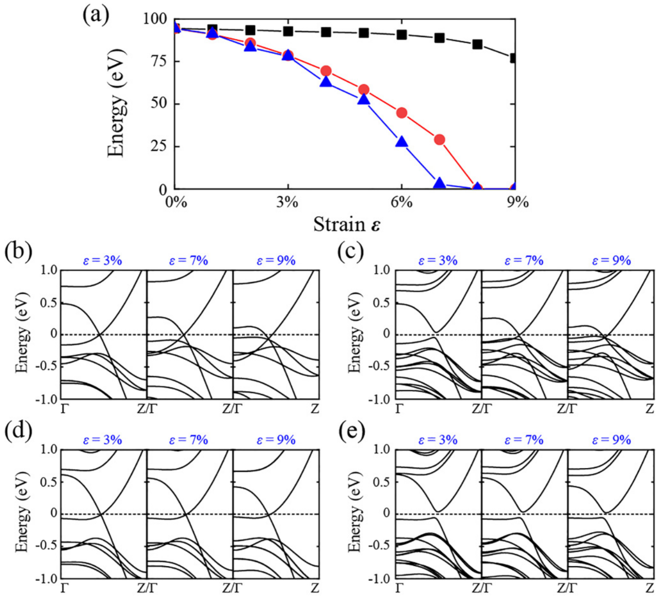

FIG. 13. (a) The band gaps of quasi-1D Nb_4SiTe_4 under strain ε, where atoms are only allowed to move in the xy plane (black), along the z axis (red), and all directions (blue). The band structures without (b) and with (c) SOC where atoms are only allowed to move along the z axis. The band structures without (d) and with (e) SOC where atoms are only allowed to move in the xy plane.

Under strain effect, both movements of atoms in the xy plane and along the z axis can result in the changing of band structures. To deeply understand this mechanism, we separately analyze the effect of the two atomic moving modes in modulating the band structures. In calculations, the atoms are only allowed to move in the xy plane or along the z axis. As shown in Fig. 13(a), both modes can result in the decreasing of band gaps. However, the effect of atomic moving along the z axis is more intense than that in the xy plane, implying that the decreasing of band gaps is the result of both modes and atomic moving along z is dominant in modulating the electronic properties. With the increase of strain, its dominant role is decreasing, which can be obtained by the increasing difference between the red and blue lines in Fig. 13(a). Nevertheless, the slope of the red line is decreasing, indicating that this individual effect is also increasing. Thus, it is concluded that the decreasing of band gaps is gradually reliant on the combination of these two atomic moving modes with the increase of strain. As shown in Figs. 13(b)–13(e), it is clear that atoms moving along the z axis can significantly modulate the band structures, causing it to resemble the normal case. This also corresponds to the conclusion above. In addition, we also investigate the influence of radius on topological properties. As shown in Fig. 14, the radius of the inner Nb atoms tube can effectively influence the inversion gap E_I. As the radius decreases, E_I decreases gradually. When it is about 2.166 Å, the band inversion vanishes and a topological phase transition from the nontrivial to the trivial occurs. Hence, it is noted that the nontrivial topological properties cannot exit with a small radius of the inner Nb atoms tube.

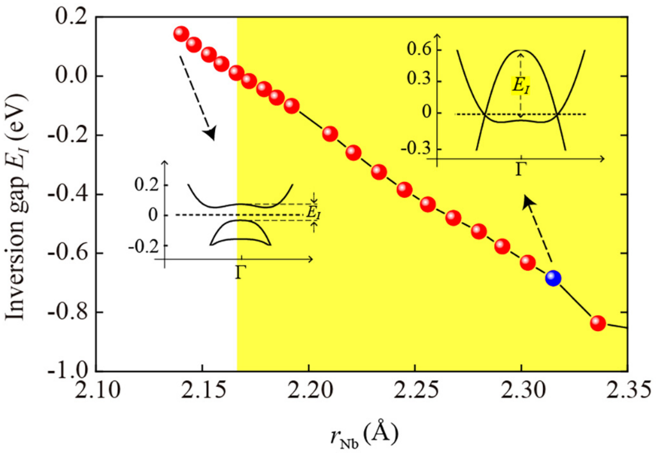

FIG. 14. The inversion gap E_I dependence on the radius of the inner Nb atoms tube without SOC effect. The yellow region indicates the intrinsic band inversion. The blue dot represents the gap at equilibrium state. The left and right insets indicate the corresponding band structures.

D. The effects of substrate, stacking, defect, and structure deformation

Since low-dimensional materials are usually carried out on substrates, it is highly considerable to explore the electronic states with substrates. Here, two candidates are considered: Graphene and *h*-BN. As shown in Fig. 15(a), the quasi-1D $\rm Nb_4SiTe_4$ nanowire is placed parallely on the substrate extending along the zigzag direction. Due to lattice mismatches, the nanowire is stretched slightly by 0.09 and 0.15 Å on graphene and *h*-BN, respectively. Simultaneously, the corresponding radius is reduced by 0.02 Å on both substrates. The distance between them is 3.39 and 3.35 Å for graphene and *h*-BN, respectively. In Figs. 15(b) and 15(c), it is clear that the band crossing can be well preserved near the Fermi level, while the SOC effect can open a gap at the degenerate Dirac point. More specifically, as shown in Fig. 15(b) for graphene, the band crossing is below the Fermi level. With SOC, it forms an electronic pocket due to the charge transfer from graphene to nanowire in Fig. 15(d). In addition, the SOC induced gaps are reduced by 9.6 and 20.1 meV, respectively, for graphene and *h*-BN, indicating that the interaction between nanowires and substrates is likely to diminish the SOC effect.

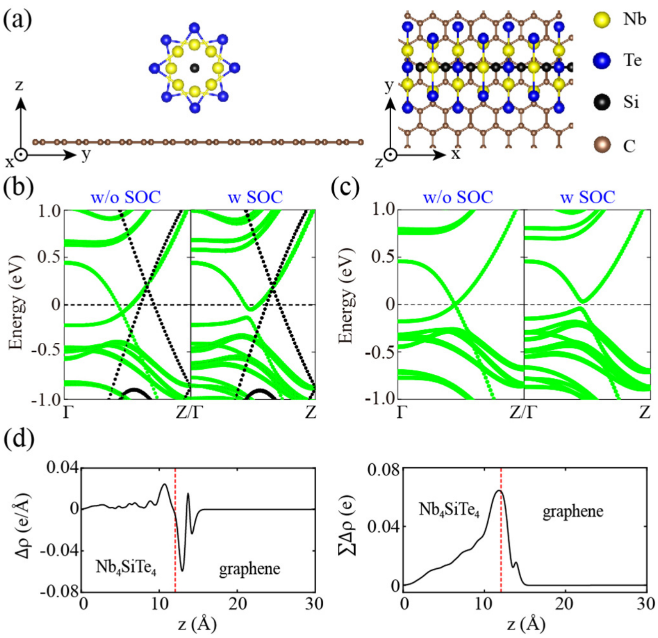

FIG. 15. (a) Front and top views of $\rm Nb_4SiTe_4$/graphene. The yellow, blue, black, and brown balls represent Nb, Te, Si, and C atoms, respectively. The band structures of $\rm Nb_4SiTe_4$/graphene (b) and $\rm Nb_4SiTe_4$/*h*-BN (c) with and without SOC effect. (d) The planar-averaged charge density difference (left panel) and its integration (right panel) along the z axis of $\rm Nb_4SiTe_4$/graphene. The red dashed line denotes the middle between $\rm Nb_4SiTe_4$ and graphene.

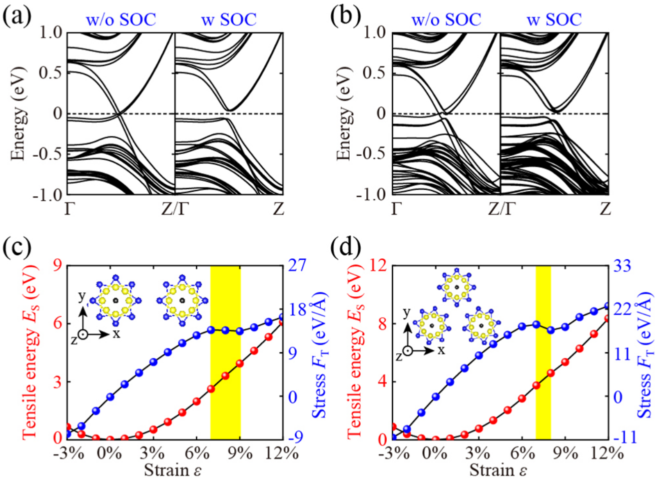

FIG. 16. The electronic band structures of two (a) and three (b) $\rm Nb_4SiTe_4$ nanowires stacking without and with the SOC effect. The black dashed line is the Fermi level at 0 eV. The strain energy E_S and tension force F_T dependencies under strain ε for two (c) and three (d) $\rm Nb_4SiTe_4$ nanowires stacking. The insets show the most stable stacking configurations. The yellow region indicates the force releasing stage.

Subsequently, the effects of stacking on electronic and mechanical properties are explored. Before evaluating electronic band structures, the most stable stacking configurations are determined in the insets of Figs. 16(c) and 16(d). In the configuration of two-nanowires stacking, four bands cross in pairs forming two Dirac points in Fig. 16(a). Likewise, when three nanowires stack together, six bands cross in pairs near the Fermi level. Due to the interaction between nanowires, only one Dirac point is formed in Fig. 16(b). In addition, the SOC opens a gap of 87.8 meV for two-nanowires stacking while 49.4 meV for three in the Fermi level. As shown in Figs. 16(c) and 16(d), the E_S increases with the enhancing strain, while the F_T is linear with ε, implying the elastic deformation stage. The Young's modulus Y_S is estimated to be 447.9 GPa (4.42×10^{-7} N) and 417.0 GPa (6.17×10^{-7} N) for two- and three-nanowire configurations, respectively. Additionally, the force releasing stage also occurs approximatively in the range of 7%–9%. These results are similar to the case of a single-nanowire system, implying the stacking has a negligible effect on the mechanical properties.

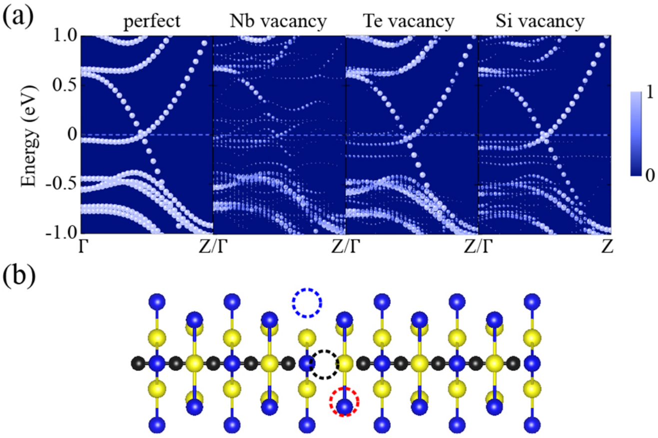

FIG. 17. (a) The band structures of Nb_4SiTe_4 without and with vacancies. The dashed line indicates the Fermi level. (b) The schematic diagram of vacancy, where blue, black, and red circles indicate Te, Si, and Nb vacancies, respectively.

Then, we turn to discuss the effects of vacancies on electronic properties. In Fig. 17(b), three kinds of vacancies of Nb, Te, and Si are considered in a fivefold supercell ($1 \times 1 \times 5$) with 90 atoms, corresponding to 2.5%, 2.5%, and 10% vacancy concentrations, respectively. The effective band structures are obtained by a band unfolding method [89,90]. As shown in Fig. 17(a), the introduction of vacancies produces several defect states near the Fermi level. However, different from the Te and Si vacancies preserving the band crossing in the Fermi level, the Nb vacancies destroy it, which can be ascribed to the complicated chemical environment around Nb atoms.

For 1D materials, the structure deformations are inescapable in actual experiments and applications. Here, to simply illustrate this effect on electronic properties, we take two cases with bending and distortion as examples. As shown in Fig. 18(a), a 20° bending can lead to the band gap opening of 81.3 meV. For the distorted mode obtained from the snapshot of AIMD simulations, the quasi-1D nanowire becomes a semiconductor with a gap of 75.3 meV in Fig. 18(b). Nevertheless, these deformation modes cannot close the band gaps, implying the remaining of the nontrivial topological phase. Around 0.2 eV above the Fermi level, it opens a large band gap of about 200 meV. These results imply the structure deformations can affect electronic properties.

IV. CONCLUSIONS

In summary, using the first-principles calculations, we predict that quasi-1D Nb_4SiTe_4 is a new TI with a sizable energy gap of 93.6 meV, large for probing the nontrivial topology experimentally. Its nontrivial band topology is examined by the nonzero $\mathbb{Z}_2$ topological invariant and zero-energy edge states in the bulk gap. Additionally, its edge states are verified robust against H decoration at boundary. We demonstrate quasi-1D Nb_4SiTe_4 harbors high tensile strength (417.2 GPa) and high elastic elongation (≈17%), indicating its excellent mechanical properties. We find, in the elastic stage, the stored strain energy can drive the different shrinking rate of the inner and outer nanotubes, which leads to the unexpected force releasing stage and expands its application in novel spintronic devices. In addition, the topological quantum phase transition from TI to trivial metal occurs at the 7% strain. Moreover, the substrate, stacking, defect, and structure deformation can specifically affect the electronic properties. Our work shows that quasi-1D Nb_4SiTe_4 provides a promising platform to study 1D topology physics and extends the family of 1D TI materials.

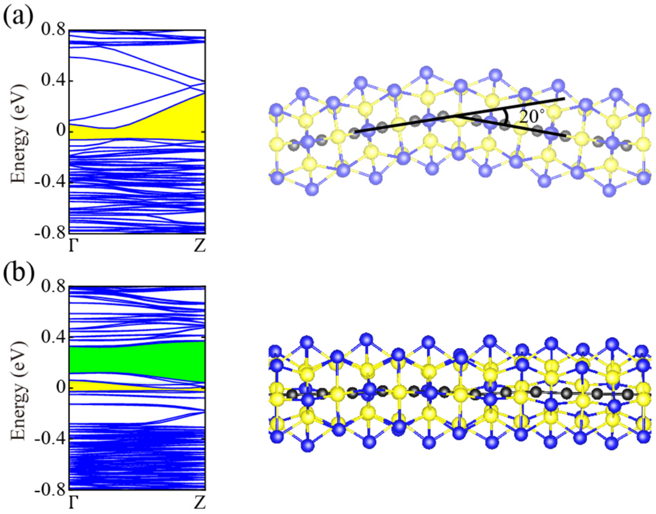

FIG. 18. The electronic structures with (a) bending and (b) distorted Nb_4SiTe_4 supercell (six cells). The yellow regions indicate the band gap in the Fermi level, while the green region indicates the new opened band gap by distortion.

ACKNOWLEDGMENTS

The authors acknowledge financial support from the National Natural Science Foundation of China (Grants No. 21603056 and No. 12104458), the Natural Science Foundation of Henan Province (Grant No. 232300421216), the Key Scientific Research Projects of the Higher Education Institutions of Henan Province (Grant No. 23A140015), the Postgraduate Talents Program of Henan University (Grant No. SYLYC2022086), and the Young Talents Program of Henan University. The numerical calculations were performed at Supercomputer Center of the China Spallation Neutron Source.

APPENDIX

The effective TB model

In order to capture the characteristics of band structures and simplify the model, the Nb d_{z^2} and Te $p_{x,y}$ orbitals are chosen to construct this model. In the primitive cell, as shown in Fig. 17(a), Ta and Te atoms in the l_1 layer belong to the Wyckoff positions $4j$ and $4n$, while in the l_2 layer, they belong to $4o$ and $4k$. Here, the Wyckoff positions $4j$, $4o$, $4n$, and $4k$ are labeled as A, B, C, and D for convenience. Then, all atomic bases can be described by $|d_{Az^2}\rangle$, $|d_{Bz^2}\rangle$, $|p_{Cx}\rangle$, $|p_{Cy}\rangle$, $|p_{Dx}\rangle$, and $|p_{Dy}\rangle$. The total effective TB model Hamiltonian considering the on-site energy, nearest-neighbor and next-nearest-neighbor hoppings under the $P/4mmm$ space group symmetry can be described as [91]

$$H_{TB}(k_z)=\begin{bmatrix} H^{AA} & 0 & H^{AC} & H^{AD} \\ 0 & H^{BB} & H^{BC} & H^{BD} \\ H^{CA} & H^{CB} & H^{CC} & 0 \\ H^{DA} & H^{DB} & 0 & H^{CD} \end{bmatrix}, \tag{A1}$$

where $H^{AA}=\varepsilon_1 I_4$, $H^{BB}=\varepsilon_2 I_4$, $H^{CC}=\begin{bmatrix}\varepsilon_3 & \\ & \varepsilon_4\end{bmatrix}\otimes I_4$, and $H^{DD}=\begin{bmatrix}\varepsilon_5 & \\ & \varepsilon_6\end{bmatrix}\otimes I_4$. The ε_1, ε_2, ε_3, ε_4, ε_5, and ε_6 are the corresponding on-site energies of $|d_{Az^2}\rangle$, $|d_{Bz^2}\rangle$, $|p_{Cx}\rangle$, $|p_{Cy}\rangle$, $|p_{Dx}\rangle$, and $|p_{Dy}\rangle$ bases, respectively. The off-diagonal block matrices including the nearest-neighbor and the next-nearest-neighbor hoppings. Because A and C are in layer l_1 while B and D are in layer l_2, there are not any k_z in H^{AC}, H^{CA}, H^{BD}, and H^{DB}. Thus the nearest-neighbor hoppings can be written as

$$H^{\mathrm{AC}}=\begin{bmatrix} t_1 & -t_2 & 0 & 0 & 0 & 0 & -t_2 & t_1 \\ t_1 & t_2 & 0 & 0 & -t_2 & -t_1 & 0 & 0 \\ 0 & 0 & -t_1 & -t_2 & 0 & 0 & t_2 & t_1 \\ 0 & 0 & -t_1 & t_2 & t_2 & -t_1 & 0 & 0 \end{bmatrix}=(H^{\mathrm{CA}})^{\dagger}, \tag{A2}$$

$$H^{\mathrm{BD}}=\begin{bmatrix} 0 & 0 & 0 & 0 & t_3 & t_4 & t_3 & -t_4 \\ -t_3 & t_4 & -t_3 & -t_4 & 0 & & 0 & 0 \\ t_4 & -t_3 & 0 & 0 & -t_4 & -t_3 & 0 & 0 \\ 0 & 0 & t_4 & t_3 & 0 & 0 & -t_4 & t_3 \end{bmatrix}=(H^{\mathrm{DB}})^{\dagger}. \tag{A3}$$

The next-nearest-neighbor hoppings can be written as

$$H^{\mathrm{AD}}=\begin{bmatrix} 0 & 0 & 0 & 0 & 0 & 0 & -\omega_1 & -\omega_1 \\ 0 & 0 & 0 & 0 & -\omega_1 & \omega_1 & 0 & 0 \\ 0 & 0 & \omega_1 & -\omega_1 & 0 & 0 & 0 & 0 \\ \omega_1 & \omega_1 & 0 & 0 & 0 & 0 & 0 & 0 \end{bmatrix}=(H^{\mathrm{DA}})^{\dagger}, \tag{A4}$$

$$H^{\mathrm{BC}}=\begin{bmatrix} \omega_2 & 0 & 0 & 0 & 0 & 0 & 0 & 0 \\ 0 & 0 & -\omega_2 & 0 & 0 & 0 & 0 & 0 \\ 0 & 0 & 0 & 0 & 0 & -\omega_2 & 0 & 0 \\ 0 & 0 & 0 & 0 & 0 & 0 & 0 & \omega_2 \end{bmatrix}=(H^{\mathrm{CB}})^{\dagger}, \tag{A5}$$

where $\omega_1=t_5e^{i(k_z/2)}$, $\omega_2=t_6e^{i(k_z/2)}$. When the SOC effect is included, the total Hamiltonian needs an additional on-site SOC term $\lambda S\cdot L$. For a d_{z^2} orbital, this term is always zero. For $p_{x,y}$ orbitals, it can be written as

$$h_{sc}=\lambda\begin{bmatrix} 0 & 0 & i & 0 \\ 0 & 0 & 0 & -i \\ -i & 0 & 0 & 0 \\ 0 & i & 0 & 0 \end{bmatrix}. \tag{A6}$$

Thus, the total Hamiltonian of the SOC term is

$$H_{so}=\lambda\begin{bmatrix} O_{2\times 2}\otimes I_8 & 0 \\ 0 & h_{sc}\otimes I_8 \end{bmatrix}. \tag{A7}$$

Based on this effective TB model, the characteristics of band inversion and degenerate Dirac-like states are captured as shown in Fig. 17(b). In particular, within the discretized k points and period gauge, the Zak phase can be calculated as

$$\gamma_n^S=\mathrm{Im}\left[\ln\prod_{i=1}^{N}\left\langle u_{nk_i}^S\middle|u_{nk_{i+1}}^S\right\rangle\right], \tag{A8}$$

where S and N represent a spin-up or spin-down channel and the number of k points.

[1] K. v. Klitzing, G. Dorda, and M. Pepper, New Method for High-Accuracy Determination of the Fine-Structure Constant Based on Quantized Hall Resistance, Phys. Rev. Lett. **45**, 494 (1980).

[2] M. Z. Hasan and C. L. Kane, *Colloquium*: Topological insulators, Rev. Mod. Phys. **82**, 3045 (2010).

[3] X.-L. Qi and S.-C. Zhang, Topological insulators and superconductors, Rev. Mod. Phys. **83**, 1057 (2011).

[4] A. Bansil, H. Lin, and T. Das, *Colloquium*: Topological band theory, Rev. Mod. Phys. **88**, 021004 (2016).

[5] H. Weng, X. Dai, and Z. Fang, Exploration and prediction of topological electronic materials based on first-principles calculations, MRS Bull. **39**, 849 (2014).

[6] P. Liu, J. R. Williams, and J. J. Cha, Topological nanomaterials, Nat. Rev. Mater. **4**, 479 (2019).

[7] D. Pesin and A. H. MacDonald, Spintronics and pseudospintronics in graphene and topological insulators, Nat. Mater. **11**, 409 (2012).

[8] D. Hsieh, D. Qian, L. Wray, Y. Xia, Y. S. Hor, R. J. Cava, and M. Z. Hasan, A topological Dirac insulator in a quantum spin Hall phase, Nature (London) **452**, 970 (2008).

[9] L. Fu and C. L. Kane, Topological insulators with inversion symmetry, Phys. Rev. B **76**, 045302 (2007).

[10] Y. L. Chen, J. G. Analytis, J. H. Chu, Z. K. Liu, S. K. Mo, X. L. Qi, H. J. Zhang, D. H. Lu, X. Dai, Z. Fang, S. C. Zhang, I. R. Fisher, Z. Hussain, and Z. X. Shen, Experimental realization of a three-dimensional topological insulator, Bi_2Te_3, Science **325**, 178 (2009).

[11] D. Hsieh, Y. Xia, D. Qian, L. Wray, J. H. Dil, F. Meier, J. Osterwalder, L. Patthey, J. G. Checkelsky, N. P. Ong, A. V. Fedorov, H. Lin, A. Bansil, D. Grauer, Y. S. Hor, R. J. Cava, and M. Z. Hasan, A tunable topological insulator in the spin helical Dirac transport regime, Nature (London) **460**, 1101 (2009).

[12] H. Zhang, C.-X. Liu, X.-L. Qi, X. Dai, Z. Fang, and S.-C. Zhang, Topological insulators in Bi_2Se_3, Bi_2Te_3 and Sb_2Te_3 with a single Dirac cone on the surface, Nat. Phys. **5**, 438 (2009).

[13] H. Lin, T. Das, Y. J. Wang, L. A. Wray, S. Y. Xu, M. Z. Hasan, and A. Bansil, Adiabatic transformation as a search tool for new topological insulators: Distorted ternary Li_2AgSb-class semiconductors and related compounds, Phys. Rev. B **87**, 121202(R) (2013).

[14] T. H. Hsieh, H. Lin, J. Liu, W. Duan, A. Bansil, and L. Fu, Topological crystalline insulators in the SnTe material class, Nat. Commun. **3**, 982 (2012).

[15] B. A. Bernevig, T. L. Hughes, and S.-C. Zhang, Quantum spin Hall effect and topological phase transition in HgTe quantum wells, Science **314**, 1757 (2006).

[16] Y. Li, P. Chen, G. Zhou, J. Li, J. Wu, B.-L. Gu, S. B. Zhang, and W. Duan, Dirac Fermions in Strongly Bound Graphene Systems, Phys. Rev. Lett. **109**, 206802 (2012).

[17] C. Weeks, J. Hu, J. Alicea, M. Franz, and R. Wu, Engineering a Robust Quantum Spin Hall State in Graphene via Adatom Deposition, Phys. Rev. X **1**, 021001 (2011).

[18] K.-H. Jin and S.-H. Jhi, Proximity-induced giant spin-orbit interaction in epitaxial graphene on a topological insulator, Phys. Rev. B **87**, 075442 (2013).

[19] S. Wang, Z. Shan, and H. Huang, The mechanical properties of nanowires, Adv. Sci. **4**, 1600332 (2017).

[20] J. Song and E. Prodan, AIII and BDI topological systems at strong disorder, Phys. Rev. B **89**, 224203 (2014).

[21] L. Li, C. Yang, and S. Chen, Winding numbers of phase transition points for one-dimensional topological systems, Europhys. Lett. **112**, 10004 (2015).

[22] K.-H. Jin and F. Liu, 1D topological phases in transition-metal monochalcogenide nanowires, Nanoscale **12**, 14661 (2020).

[23] G. Autès, A. Isaeva, L. Moreschini, J. C. Johannsen, A. Pisoni, R. Mori, W. Zhang, T. G. Filatova, A. N. Kuznetsov, L. Forrò, W. V. den Broek, Y. Kim, K. S. Kim, A. Lanzara, J. D. Denlinger, E. Rotenberg, A. Bostwick, M. Grioni, and O. V. Yazyev, A novel quasi-one-dimensional topological insulator in bismuth iodide $\beta-Bi_4I_4$, Nat. Mater. **15**, 154 (2016).

[24] T. Pham, S. Oh, S. Stonemeyer, B. Shevitski, J. D. Cain, C. Song, P. Ercius, M. L. Cohen, and A. Zettl, Emergence of Topologically Nontrivial Spin-Polarized States in a Segmented Linear Chain, Phys. Rev. Lett. **124**, 206403 (2020).

[25] W. P. Su, J. R. Schrieffer, and A. J. Heeger, Soliton excitations in polyacetylene, Phys. Rev. B **22**, 2099 (1980).

[26] T. Y. Yang, Q. Wan, D. Y. Yan, Z. Zhu, Z. W. Wang, C. Peng, Y. B. Huang, R. Yu, J. Hu, Z. Q. Mao, Si Li, Shengyuan A. Yang, H. Zheng, J. F. Jia, Y. G. Shi, and N. Xu, Directional massless Dirac fermions in a layered van der Waals material with one-dimensional long-range order, Nat. Mater. **19**, 27 (2020).

[27] J. Hu, X. Liu, C. L. Yue, J. Y. Liu, H. W. Zhu, J. B. He, J. Wei, Z. Q. Mao, L. Y. Antipina, Z. I. Popov, P. B. Sorokin, T. J. Liu, P. W. Adams, S. M. A. Radmanesh, L. Spinu, H. Ji, and D. Natelson, Enhanced electron coherence in atomically thin Nb_3SiTe_6, Nat. Phys. **11**, 471 (2015).

[28] M. Zhao, W. Xia, Y. Wang, M. Luo, Z. Tian, Y. Guo, W. Hu, and J. Xue, Nb_2SiTe_4: A stable narrow-gap two-dimensional material with ambipolar transport and mid-infrared response, ACS Nano **13**, 10705 (2019).

[29] B. Wang, W. Xia, S. Li, K. Wang, S. A. Yang, Y. Guo, and J. Xue, One-dimensional metal embedded in two-dimensional semiconductor in $Nb_2Si_{x-1}Te_4$, ACS Nano **15**, 7149 (2021).

[30] Y. Yoshikawa, T. Wada, Y. Okamoto, Y. Abe, and K. Takenaka, Large thermoelectric power factor in whisker crystals of solid solutions of the one-dimensional tellurides Ta_4SiTe_4 and Nb_4SiTe_4, Appl. Phys. Express **13**, 125505 (2020).

[31] K. Ahn, T. Hughbanks, K. D. D. Rathnayaka, and D. G. Naugle, Electrical properties of the square-antiprismatic chain compounds M_4Br_4Os (M = Y, Er) and M_4Te_4Z (M = Nb, Ta; Z = Si, Cr, Fe, Co), Chem. Mater. **6**, 418 (1994).

[32] S. Liu, H. Yin, D. J. Singh, and P.-F. Liu, Ta_4SiTe_4: A possible one-dimensional topological insulator, Phys. Rev. B **105**, 195419 (2022).

[33] G. Kresse and J. Hafner, *Ab initio* molecular dynamics for liquid metals, Phys. Rev. B **47**, 558 (1993).

[34] G. Kresse and J. Hafner, *Ab initio* molecular-dynamics simulation of the liquid-metal–amorphous-semiconductor transition in germanium, Phys. Rev. B **49**, 14251 (1994).

[35] J. P. Perdew, K. Burke, and M. Ernzerhof, Generalized Gradient Approximation Made Simple, Phys. Rev. Lett. **77**, 3865 (1996).

[36] G. Kresse and D. Joubert, From ultrasoft pseudopotentials to the projector augmented-wave method, Phys. Rev. B **59**, 1758 (1999).

[37] S. Grimme, J. Antony, S. Ehrlich, and H. Krieg, A consistent and accurate *ab initio* parametrization of density functional dispersion correction (DFT-D) for the 94 elements H-Pu, J. Chem. Phys. **132**, 154104 (2010).

[38] A. Togo and I. Tanaka, First principles phonon calculations in materials science, Scr. Mater. **108**, 1 (2015).

[39] S. Nosè, A unified formulation of the constant temperature molecular dynamics methods, J. Chem. Phys. **81**, 511 (1984).

[40] D. Bucher, L. C. T. Pierce, J. A. McCammon, and P. R. L. Markwick, On the use of accelerated molecular dynamics

to enhance configurational sampling in *ab initio* simulations, J. Chem. Theory Comput. **7**, 890 (2011).

[41] G. Kresse and J. Furthmüller, Efficient iterative schemes for *ab initio* total-energy calculations using a plane-wave basis set, Phys. Rev. B **54**, 11169 (1996).

[42] G. Pizzi, V. Vitale, R. Arita, S. Blugel, F. Freimuth, G. Geranton, M. Gibertini, D. Gresch, C. Johnson, T. Koretsune, J. Ibanez-Azpiroz, H. Lee, J. M. Lihm, D. Marchand, A. Marrazzo, Y. Mokrousov, J. I. Mustafa, Y. Nohara, Y. Nomura, L. Paulatto *et al.*, Wannier90 as a community code: New features and applications, J. Phys.: Condens. Matter **32**, 165902 (2020).

[43] Q. Wu, S. Zhang, H.-F. Song, M. Troyer, and A. A. Soluyanov, WannierTools: An open-source software package for novel topological materials, Comput. Phys. Commun. **224**, 405 (2018).

[44] V. Wang, N. Xu, J.-C. Liu, G. Tang, and W.-T. Geng, VASPKIT: A user-friendly interface facilitating high-throughput computing and analysis using VASP code, Comput. Phys. Commun. **267**, 108033 (2021).

[45] M. E. Badding, R. L. Gitzendanner, R. P. Ziebarth, and F. J. DiSalvo, Electrical and magnetic properties of tantalum silicon telluride and isostructural compounds, Mater. Res. Bull. **29**, 327 (1994).

[46] M. E. Badding and F. J. DiSalvo, Synthesis and structure of tantalum silicide telluride, Ta_4SiTe_4, a new low-dimensional material, Inorg. Chem. **29**, 3952 (1990).

[47] J. Li, R. Hoffmann, M. E. Badding, and F. J. DiSalvo, Electronic and structural properties of the novel chain compound tantalum telluride silicide, Ta_4Te_4Si, Inorg. Chem. **29**, 3943 (1990).

[48] R. Sen and P. Johari, One-dimensional-Sn_2X_3 ($X = S$, Se) as promising optoelectronic and thermoelectronic materials: A comparison with three-dimensional-Sn_2X_3, ACS Appl. Mater. Interfaces **11**, 12733 (2019).

[49] H. O. H. Churchill, G. J. Salamo, S.-Q. Yu, T. Hironaka, Xian Hu, J. Stacy, and I. Shih, Toward single atom chains with exfoliated tellurium, Nanoscale Res. Lett. **12**, 488 (2017).

[50] F. Lu, J. Cui, P. Liu, M. Lin, Y. Cheng, H. Liu, W. Wang, K. Cho, and W.-H. Wang, High-throughput identification of one-dimensional atomic wires and first principles calculations of their electronic states, Chin. Phys. B **30**, 057304 (2021).

[51] S.-s. Li, Y.-p. Wang, S.-j. Hu, D. Chen, C.-w. Zhang, and S.-s. Yan, Robust half-metallicity in transition metal tribromide nanowires, Nanoscale **10**, 15545 (2018).

[52] X. Tan, L. Liu, H. Xiang, G.-F. Du, A. Lou, and H.-H. Fu, One-dimensional transition metal dihalide nanowires as robust bipolar magnetic semiconductors, Nanoscale **12**, 8942 (2020).

[53] D. F. Souza, A. L. Rosa, P. Venezuela, J. E. Padilha, A. Fazzio, and R. B. Pontes, Structural evolution and the role of native defects in subnanometer MoS nanowires, Phys. Rev. B **100**, 235416 (2019).

[54] S. Jiang, H. Yin, G.-P. Zheng, B. Wang, S. Guan, and B.-J. Yao, Computational prediction of a novel 1D InSeI nanochain with high stability and promising wide-bandgap properties, Phys. Chem. Chem. Phys. **22**, 27441 (2020).

[55] R. F. W. Bader, *Atoms in Molecules: A Quantum Theory* (Oxford University Press, Oxford, 1990).

[56] P. Schwerdtfeger and J. K. Nagle, 2018 table of static dipole polarizabilities of the neutral elements in the periodic table, Mol. Phys. **117**, 1200 (2019).

[57] A. D. Becke and K. E. Edgecombe, A simple measure of electron localization in atomic and molecular systems, J. Chem. Phys. **92**, 5397 (1990).

[58] A. Savin, A. D. Becke, J. Flad, R. Nesper, H. Preuss, and H. G. von Schnering, A new look at electron localization, Angew. Chem., Int. Ed. Engl. **30**, 409 (1991).

[59] A. H. Castro Neto, F. Guinea, N. M. R. Peres, K. S. Novoselov, and A. K. Geim, The electronic properties of graphene, Rev. Mod. Phys. **81**, 109 (2009).

[60] X. Qian, J. Liu, L. Fu, and J. Li, Quantum spin Hall effect in two-dimensional transition metal dichalcogenides, Science **346**, 1344 (2014).

[61] S. Tang, C. Zhang, D. Wong, Z. Pedramrazi, H.-Z. Tsai, C. Jia, B. Moritz, M. Claassen, H. Ryu, S. Kahn, J. Jiang, H. Yan, M. Hashimoto, D. Lu, R. G. Moore, C.-C. Hwang, C. Hwang, Z. Hussain, Y. Chen, M. M. Ugeda *et al.*, Quantum spin Hall state in monolayer 1T'-WTe_2, Nat. Phys. **13**, 683 (2017).

[62] H. Zhang and S.-C. Zhang, Topological insulators from the perspective of first-principles calculations, Phys. Status Solidi RRL **7**, 72 (2013).

[63] Z. Zhu, Y. Cheng, and U. Schwingenschlögl, Band inversion mechanism in topological insulators: A guideline for materials design, Phys. Rev. B **85**, 235401 (2012).

[64] Y. Ma, L. Kou, X. Li, Y. Dai, and T. Heine, Two-dimensional transition metal dichalcogenides with a hexagonal lattice: Room-temperature quantum spin Hall insulators, Phys. Rev. B **93**, 035442 (2016).

[65] N. Marzari, A. A. Mostofi, J. R. Yates, I. Souza, and D. Vanderbilt, Maximally localized Wannier functions: Theory and applications, Rev. Mod. Phys. **84**, 1419 (2012).

[66] J. Zak, Berry's Phase for Energy Bands in Solids, Phys. Rev. Lett. **62**, 2747 (1989).

[67] S.-C. Zhang, Topological insulators, Scholarpedia **10**, 30275 (2015).

[68] Y. Ando, Topological insulator materials, J. Phys. Soc. Jpn. **82**, 102001 (2013).

[69] X.-G. Wen, Topological orders and edge excitations in fractional quantum Hall states, Adv. Phys. **44**, 405 (1995).

[70] B. T. Wang, Y. Cheng, and E. R. Margine, Evolution of the topologically protected surface states in superconductor $\beta-Bi_2Pd$ from the three-dimensional to the two-dimensional limit, J. Phys.: Condens. Matter **29**, 325501 (2017).

[71] S. Nie, L. Xing, R. Jin, W. Xie, Z. Wang, and F. B. Prinz, Topological phases in the $TaSe_3$ compound, Phys. Rev. B **98**, 125143 (2018).

[72] Z. Guo, D. Yan, H. Sheng, S. Nie, Y. Shi, and Z. Wang, Quantum spin Hall effect in $Ta_2M_3Te_5$ ($M =$ Pd, Pt, Ni), Phys. Rev. B **103**, 115145 (2021).

[73] C. Zhao, M. Hu, J. Qin, B. Xia, C. Liu, S. Wang, D. D. Guan, Y. Li, H. Zheng, J. Liu, and J. Jia, Strain Tunable Semimetal–Topological-Insulator Transition in Monolayer 1T-WTe_2, Phys. Rev. Lett. **125**, 046801 (2020).

[74] H. Zhang, W. Yang, Y. Wang, and X. Xu, Tunable topological states in layered magnetic materials of $MnSb_2Te_4$, $MnBi_2Se_4$, and $MnSb_2Se_4$, Phys. Rev. B **103**, 094433 (2021).

[75] Y. Wu, W. Sun, S. Liu, B. Wang, C. Liu, H. Yin, and Z. Cheng, $Ni(NCS)_2$ monolayer: A robust bipolar magnetic semiconductor, Nanoscale **13**, 16564 (2021).

[76] B. I. Yakobson, C. J. Brabec, and J. Bernholc, Nanomechanics of Carbon Tubes: Instabilities beyond Linear Response, Phys. Rev. Lett. **76**, 2511 (1996).

[77] M. Topsakal and S. Ciraci, Elastic and plastic deformation of graphene, silicene, and boron nitride honeycomb nanoribbons under uniaxial tension: A first-principles density-functional theory study, Phys. Rev. B **81**, 024107 (2010).

[78] C. Ott, F. Reiter, M. Baumgartner, M. Pielmeier, A. Vogel, P. Walke, S. Burger, M. Ehrenreich, G. Kieslich, D. Daisenberger, J. Armstrong, U. K. Thakur, P. Kumar, S. Chen, L. S. Donadio, D. Walter, R. T. Weitz, K. Shankar, and T. Nilges, Flexible and ultrasoft inorganic 1D semiconductor and heterostructure systems based on SnIP, Adv. Funct. Mater. **29**, 1900233 (2019).

[79] I. Kaplan-Ashiri, S. R. Cohen, K. Gartsman, R. Rosentsveig, G. Seifert, and R. Tenne, Mechanical behavior of individual WS_2 nanotubes, J. Mater. Res. **19**, 454 (2004).

[80] M. M. Shokrieh and R. Rafiee, A review of the mechanical properties of isolated carbon nanotubes and carbon nanotube composites, Mech. Compos. Mater. **46**, 155 (2010).

[81] E. Hernández, C. Goze, P. Bernier, and A. Rubio, Elastic properties of single-wall nanotubes, Appl. Phys. A **68**, 287 (1999).

[82] K. Chandraseker and S. Mukherjee, Atomistic-continuum and *ab initio* estimation of the elastic moduli of single-walled carbon nanotubes, Comput. Mater. Sci. **40**, 147 (2007).

[83] G. Van Lier, C. Van Alsenoy, V. Van Doren, and P. Geerlings, *Ab initio* study of the elastic properties of single-walled carbon nanotubes and graphene, Chem. Phys. Lett. **326**, 181 (2000).

[84] T. W. Tombler, C. Zhou, L. Alexseyev, J. Kong, H. Dai, L. Liu, C. S. Jayanthi, M. Tang, and S.-Y. Wu, Reversible electromechanical characteristics of carbon nanotubes under local-probe manipulation, Nature (London) **405**, 769 (2000).

[85] A. Cao, Y. Wei, and E. Ma, Grain boundary effects on plastic deformation and fracture mechanisms in Cu nanowires: Molecular dynamics simulations, Phys. Rev. B **77**, 195429 (2008).

[86] S. Ogata, J. Li, and S. Yip, Ideal pure shear strength of aluminum and copper, Science **298**, 807 (2002).

[87] R. Agrawal, B. Peng, and H. D. Espinosa, Experimental-computational investigation of ZnO nanowires strength and fracture, Nano Lett. **9**, 4177 (2009).

[88] S. Narayanan, G. Cheng, Z. Zeng, Y. Zhu, and T. Zhu, Strain hardening and size effect in five-fold twinned Ag nanowires, Nano Lett. **15**, 4037 (2015).

[89] V. Popescu and A. Zunger, Effective Band Structure of Random Alloys, Phys. Rev. Lett. **104**, 236403 (2010).

[90] V. Popescu and A. Zunger, Extracting e versus k effective band structure from supercell calculations on alloys and impurities, Phys. Rev. B **85**, 085201 (2012).

[91] Z. Zhang, Z.-M. Yu, G.-B. Liu, and Y. Yao, MagneticTB: A package for tight-binding model of magnetic and non-magnetic materials, Comput. Phys. Commun. **270**, 108153 (2022).